

Numerical simulation and experimental investigations of the 3D simultaneous heat and mass transfer in a drying system operating under forced convection mode

Clement A. Komolafe^{1}, Omotola J. Komolafe², Albert K. Arkoh³, Fuseini Mumuni⁴, Frederick A. Akendola¹ and Eugene Apiiga¹*

¹Department of Mechanical Engineering, Faculty of Engineering, University of Mines and Technology, P.O.B. 237, Tarkwa, Ghana, West Africa.

²Electrical Section, Engineering /Maintenance Department, Cocoa Research Institute of Nigeria, Ibadan, Nigeria.

³Department of Mechanical Engineering, Faculty of Engineering, Takoradi Technical University, P.O.B. 256, Takoradi, Ghana.

⁴Department of Electrical and Electronic Engineering, Faculty of Engineering, University of Mines and Technology, P.O.B. 237, Tarkwa Ghana, West Africa.

Abstract. Drying agricultural products and other porous media is typically done in the open sun, which is unhygienic, labour intensive, and dependent on varying weather conditions. Designing an efficient drying system requires a comprehensive computational analysis of relevant drying phenomena. In this study, numerical simulations and experimental investigations of three-dimensional simultaneous heat and mass transfer in a photovoltaic (PV) - powered drying system operating under forced convection were conducted under no load conditions. The equations governing continuity, momentum, energy, and species were solved using ANSYS Fluent's Finite Volume Method (FVM), a computational fluid dynamics tool. The highest simulated temperature and velocity in the drying chamber, 393 K and 1.55 m/s, respectively, closely matched the experimental values of 386 K and 1.40 m/s. It is recommended that the developed drying system serve as a practical alternative to traditional open sun drying, as the numerical results were within an acceptable range.

* Corresponding author: cakomolafe@umat.edu.gh

1 Introduction

The leading cause of food shortages after harvest in most developing countries worldwide is a lack of sustainable preservation methods. To balance global food resources with population growth, post-harvest losses at various points in the food supply chain must be reduced through the adoption of advanced preservation techniques and industrial solutions (Saha et al., 2024). There are various methods for preserving foodstuffs and other agricultural products, including drying, refrigeration, frying, salting, canning, pasteurization, and fermentation. Among these, drying is a commonly used preservation method because it reduces moisture content, which helps prevent biochemical, chemical, and microbiological deterioration (Vásquez et al., 2019).

Drying is an essential step in many agricultural and industrial processes, reducing the moisture content of products so they can be processed further. As a key operation in numerous industrial applications, drying is a vital, energy-intensive process that involves complex heat and mass transfer (Komolafe, 2023). Traditionally, drying is often done using fossil fuels or the open sun. Most agricultural products are dried outdoors, either in the sun or shade, in rural and some urban areas worldwide, because no other drying options are available. In open sun drying, the product is spread on the ground or another surface exposed to solar radiation; thus, it is subjected to wind and sunlight, which dry it in an uncontrolled manner. Although open sun drying has proven to be the most affordable and efficient method for drying many agricultural products, such as medicinal plants and food crops, it has drawbacks. These include longer drying times and lower-quality products due to inevitable rain, insect infestations, and wind. As global energy demand increases and the harmful effects of fossil fuel use become more apparent, there is a growing need for accessible, environmentally friendly energy sources. Because solar energy is abundant and renewable, it particularly presents a promising alternative.

It is widely used as a renewable energy source across various applications due to its low maintenance costs, a small carbon footprint, and simple infrastructure requirements.

Because of its abundance in nature, solar energy has attracted significant interest from developed, developing, and emerging economies as they seek to use renewable sources to fight climate change. It is also seen as a crucial energy resource worldwide for the future, given the limited and sparse reserves of other renewables and the environmental issues associated with fossil fuels and their finite supplies. Photovoltaic (PV) technology and concentrating solar power systems are two methods for harnessing solar energy, either directly or indirectly utilizing solar energy (Chukwujindu, 2017). Photovoltaic technology and applications have been the most cost-effective green energy resource, especially in tropical regions of the world. (Hammami et al., 2017; Ya'acob et al., 2013). The ability to generate thermal and electrical

energy simultaneously makes photovoltaic-thermal systems the most popular type of solar energy systems

The UN's global initiative to increase renewable energy use has encouraged many countries, businesses, and individuals to adopt solar photovoltaic (PV) systems to harness solar energy. (Dhonde et al., 2022). In agriculturally viable regions like West Africa, solar energy is a clean, renewable source that offers a reliable and excellent alternative for powering mechanized agricultural equipment due to its abundance, sustainability, and environmental friendliness (Agbor et al., 2023). A major step toward incorporating solar PV into farming machinery and eliminating greenhouse gas (GHG) emissions from the environment is mechanized agriculture (Dhonde et al., 2022). Several solar PV systems have been integrated into machines used for various processes, including pod splitting, irrigation, drying, threshing, shelling, frying, and cooking.

The use of numerical methods and computational fluid dynamics (CFD) tools to model and simulate the drying kinetics of agricultural goods is one of the technological approaches used to examine the drying process. The application of CFD techniques is essential for better system design.

Additionally, modeling and simulation are essential for better design, and computer simulation offers a cost-effective, time-saving, and energy efficient way to obtain detailed, reasonably accurate information about food processing operations. Through computer simulation, comprehensive and fairly precise data about food processing activities can also be obtained. The 3D data offers a more comprehensive physical insight into the drying process, potentially sparking innovative redesigns or enhancements. Additionally, analyzing with a 3D model can expose the complete thermal profile of the drying system. While the numerical approach has many benefits over analytical or experimental methods, the full adoption of CFD techniques for predicting heat and mass transfer in PV controlled drying processes remains limited.

Although there are studies on numerical analysis of PV powered machines/equipment, such as drying systems (Chouchane et al., 2025; Rabah et al., 2025; Tuncer et al., 2023; Variava et al., 2024; Wang et al., 2025), cooling (Alqatamin & Jinzhan, 2025; Utomo et al., 2025), and concentrated photovoltaic thermal systems (Variava et al., 2024). However, information on the CFD-based analysis of 3D simultaneous heat and mass transfer for a solar PV-powered drying system capable of providing electrical and thermal energy and continuously stirring the products on the drying tray without human contact is scarce. Therefore, the specific goal of this study is to evaluate the 3D simultaneous heat and mass transfer in a PV powered drying system operating under forced convection mode for thermal evaluation using both numerical and experimental methods.

2 Materials and Methods

Table 1: Specifications and sensitivities of measuring devices

Measuring Devices	Measured parameters	Model	Range
Solarimeter	Irradiation	SM206	0.1 - 1999.9 W/m ²
Multi-channel temperature meter	Temperature	K-Type Model: AT 4028	0-200 °C
Anemometer	Air velocity	816-EN-00	0-30 m/s 10% RH ~ 99%
Humidity Meter	Temperature/ Humidity	LO01	RH

2.1 Solar drying system geometry, description and data measurement

The 3D geometry used to model the PV powered drying system is shown schematically in Figure 1. It includes a stainless steel drying platform with a 4 kg tray capacity (measuring 718 x 348 x 35 mm), an insulated double-wall stainless steel drying chamber (measuring 808 x 438 x 648 mm), three 300 W heating elements (totaling 900 W) arranged in front of the blower to heat incoming air, along with the blower, a 1 hp DC motor, and a base frame. No-load experimental tests were conducted using the 900 W heating elements at the Institute of Agricultural Research and Training, Moor Plantation, Ibadan, Nigeria, from 9:00 to 18:00 on five days, at a latitude of 7° 4' and longitude of 3° 9', to determine the thermal profiles of the drying systems. According to the design specifications, the PV system for the experimental setup includes four 250 W solar panels, four 120 Ah lithium batteries, and a 50 Amp charge controller. The temperatures within the drying chamber, ambient air, and outlet were measured hourly using a multi-channel temperature meter (AX 4202). During the experiments, data on solar radiation, air velocity, humidity, and ambient temperature were recorded hourly using devices such as a pyranometer, an anemometer, and a humidity meter. The specifications of these measuring instruments are shown in Table 1. The average values of these parameters were then calculated. All connections among these components were securely sealed to minimize infiltration losses.

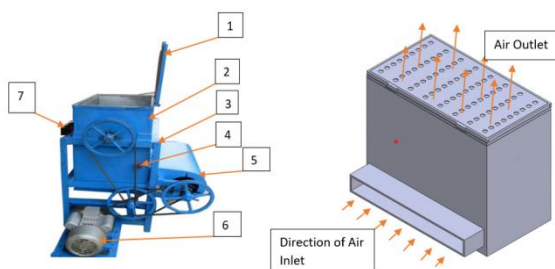


Fig.1. Pictorial and schematic view of the experimental setup. 1. Cover with a handle 2. Drying chamber 3. Supporting frame 4. Thermostat 5. Blower housing 6. Electric motor 7. Switches

2.2 Mathematical model for the turbulent air flow

The CFD approach was employed to study the interactions and movement of numerous individual particles within the fluid domain. (Vyas, 2017). It involves numerically solving non-linear partial differential equations that describe convective fluid motion within a 3D object, including the equations of mass (continuity), momentum, and energy. (Komolafe et al., 2019; Romero et al., 2014). The governing equations are summarised as follows (Komolafe, 2023)

The equation (Navier Stokes) governing the force convection airflow inside the dryer is expressed by (Lemus-Mondaca et al., 2017; Zambra et al., 2012)

$$\frac{\partial}{\partial t}(\rho u_i) + \frac{\partial}{\partial x_j}(\rho u_j u_i) = \frac{\partial \rho}{\partial x_i} + \frac{\partial \tau_{ij}}{\partial x_i} - \rho g \delta_{ij} \quad (1)$$

where u_i is the vector field velocity, ρ is the density of air, p is the pressure, τ_{ij} is the deviatoric stress tensor. The last term represents the body force. It is related to g , which is the gravitational acceleration. δ is Kronecker delta, i and j are Cartesian coordinates indices. In addition, the flow must satisfy the mass conservation as follows:

Continuity equation

$$\frac{\partial \rho}{\partial t} + \frac{\partial}{\partial x_i}(\rho u_i) = 0 \quad (2)$$

These equations are solved in Reynolds-averaged form. The flow is regarded as quasi-incompressible (i.e., low-Mach number approximation) but with variable density. Density variations are directly linked to pressure in this situation, but they are also linked to temperature variations. It suggests that all density-velocity correlations and a few dilatational elements in the Navier-Stokes equations' Reynolds decomposition are insignificant. Consequently, the Reynolds-averaged governing equations become (Lemus-Mondaca et al., 2017; Zambra et al., 2012)

Linear momentum equation

$$\frac{\partial}{\partial t}(\bar{\rho} \bar{u}_i) + \frac{\partial}{\partial x_j}(\bar{\rho} \bar{u}_j \bar{u}_i) = \frac{\partial \bar{p}}{\partial x_i} + \frac{\partial}{\partial x_j} \left[\mu + \mu_t \left(\frac{\partial \bar{u}_i}{\partial x_j} + \frac{\partial \bar{u}_j}{\partial x_i} \right) \right] - \bar{\rho} g \delta_{ij} \quad (3)$$

and

$$\frac{\partial \bar{p}}{\partial x_i} + \frac{\partial}{\partial x_j}(\bar{\rho} \bar{u}_i) = 0 \quad (4)$$

Turbulent stresses have been taken into consideration by varying turbulent viscosity u_t , with bars representing

temporal averages. The isotropic component of the turbulent stress tensor is included in the pressure term.

The turbulent viscosity is determined using the rate of dissipation (ε) and the turbulent kinetic energy (κ), which may be described using dimensional arguments as follows:

$$\mu_t = \rho C_u \frac{\kappa^2}{\varepsilon} \quad (5)$$

where C_u is considered to be phenomenological constant. The variables κ and ε can be obtained by solving the pertinent transport equations.

The equation for turbulent kinetic energy

$$\frac{\partial}{\partial t} (\bar{\rho} \kappa_i) + \frac{\partial}{\partial x_j} (\bar{\rho} \bar{u}_j \kappa) = \frac{\partial}{\partial x_i} \left[\left(\frac{\mu + \mu_t}{\sigma_\kappa} \right) \frac{\partial \kappa}{\partial x_j} \right] + G - \bar{\rho} \varepsilon \quad (6)$$

For the turbulent kinetic energy (air), dissipation rate equation is expressed as:

$$\frac{\partial}{\partial t} (\bar{\rho} \varepsilon_i) + \frac{\partial}{\partial x_j} (\bar{\rho} \bar{u}_j \varepsilon) = \frac{\partial}{\partial x_i} \left[\left(\frac{\mu + \mu_t}{\sigma_\varepsilon} \right) \frac{\partial \varepsilon}{\partial x_j} \right] + G C_1 \frac{\varepsilon}{\kappa} - C_2 \bar{\rho} \frac{\varepsilon^2}{\kappa} \quad (7)$$

The following expression describes the rate at which the mean-flow velocity gradient tensor interacts with turbulent stresses to produce turbulent kinetic energy, which is represented by the quantity G in Equation (6):

$$G = \mu + \mu_t \left(\frac{\partial \bar{u}_i}{\partial \bar{x}_j} + \frac{\partial \bar{u}_j}{\partial \bar{x}_i} \right) \frac{\partial \bar{u}_j}{\partial \bar{x}_i} \quad (8)$$

While the corresponding Prandtl numbers for turbulent kinetic energy dissipation and diffusion are σ_ε and σ_κ , respectively, the model's closure constants are C_1 and C_2 . The typical κ - ε model specifies them as follows (Launder & Spalding, 1983)

$$C_1 = 1.44; C_2 = 1.9; C_u = 0.1; \sigma_\kappa = 1.0; \sigma_\varepsilon = 1.212 \quad (9)$$

Thermal energy can be stated as shown in eqn. (12)

Understanding the turbulent Prandtl and Schmidt numbers is necessary to calculate turbulent heat and mass transfer in air (Lemus-Mondaca et al., 2017):

$$t = \frac{\mu_t}{\sigma_t} \quad (10)$$

$$\text{where } \sigma_t = \begin{cases} pr(\phi = T) \\ Sc(\phi = T) \end{cases} \quad 0.5 \leq \sigma_t \leq 1.0 \quad (11)$$

$$\frac{\partial}{\partial t} (\bar{\rho} T) + \frac{\partial}{\partial x_j} (\bar{\rho} \bar{u}_j T) = \frac{\partial}{\partial x_i} \left[\left(\kappa + \frac{\mu_t}{\sigma_t} \right) \frac{\partial T}{\partial x_j} \right] \quad (12)$$

where κ is the air's molecular thermal diffusion coefficient and is the temperature's turbulent thermal Prandtl number σ_t . Since air is considered an ideal gas combination, the ideal gas law can be used to calculate the mean density.

2.3 Development of model geometry

The PV-powered drying system's computer model was developed and meshed with ANSYS Fluent software to predict the thermal profile of the drying process, as illustrated in Figure 2.

2.4 Assumptions

The following were the assumptions for the computational analysis (Komolafe, 2023; Komolafe et al., 2022)

- For the operational range, the flow is constant, three-dimensional, and incompressible;
- The geometry of the solar drying systems is assumed to be symmetrical;
- Air's thermophysical characteristics remain constant;
- The drying systems are assumed to operate under no load conditions;
- No drying tray;
- No slip condition.

2.5 Boundary Conditions

Several suitable initial values and boundary criteria were used to determine the bounds of the computation domain. The domain has one pressure exit and one mass flow inlet. The airflow was directed perpendicular to the inlet, as illustrated in Figure 1. Material properties are detailed in Table 2. It was also believed that the air was at room temperature. This is how the starting and boundary conditions are explained (Rani & Tripathy, 2023):

A temperature inlet air boundary condition and a velocity boundary condition were applied at the drying chamber inlet section.

$$u = U_{in}, v = w = 0, T = T_{in} \quad (13)$$

where, U_{in} is the average air velocity

The outlet section of the drying system was expressed in terms of atmospheric pressure.

$$p = p_{at} \quad (14)$$

No slip boundary condition:

$$u = v = w = 0 \quad (15)$$

Table 2: Thermophysical properties used in the CFD analysis for Air

Property	Air
----------	-----

Density (ρ) (kg/m ³)	1.293
Specific Heat (C_p) (J/kg/K)	1005
Thermal Conductivity (k) (W/mK)	0.0262
Viscosity (μ) (kg/m/s)	1.604×10^{-5}

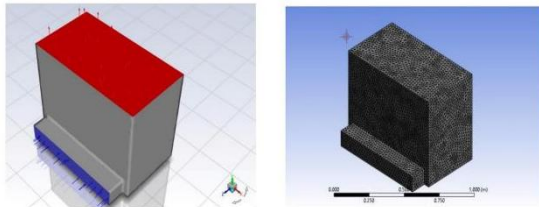


Fig.2. 3D geometry and meshing models of the drying system

2.6 Simulation procedure

The simulation process in this study was carried out using the approach (Komolafe et al., 2022). The partial differential equations describing the thermal behaviour of the three-dimensional (3D) drying system were numerically solved using ANSYS Fluent version 2023 R1 CFD software, with the standard k- ϵ (k-epsilon) turbulence model and initial and boundary conditions applied. The standard k- ϵ model, combined with scalable wall functions, was used to simulate turbulence transport by the mean flow and diffusion within the solar drying system. It was chosen for its higher predictive accuracy compared to models like k-omega, Spalart-Allmaras, and Large Eddy Simulation. Figure 2 shows the 3D geometry and mesh of the drying system. During mesh generation, the PV-powered drying system's domains, especially the drying chamber, were meshed using conventional methods to minimize computation time. The geometry was meshed in ANSYS Workbench using tetrahedral elements, resulting in an unstructured mesh suited to the complex geometry and small elements for detail. Unstructured meshing is recommended for its flexibility, especially for curved and irregular boundaries that are difficult to mesh with structured approaches. The domain contains 115482 tetrahedral elements, with sizes ranging from 0.06415 to 6.6530. It was also believed that the air was at room temperature. This is how each governing equation continuity, momentum, energy, and species is transformed into a linear algebraic form through discretization using the Finite Volume Method (FVM). These equations were solved using the SIMPLEC (Semi-Implicit Method for Pressure-linked Equations-Consistent) technique, which ensures good convergence, particularly for strongly coupled situations.

2.7 Grid Independent Test

To find the ideal mesh resolution for an accurate CFD model while reducing computing time, grid independence research was carried out. The studied domain was created, and the solution domain was discretized based on the

element's size. Air velocity and temperature were calculated at each grid point. Throughout the simulation, the applied boundary conditions were kept constant to guarantee precise result comparison. At 106,642 elements, the air velocity and temperature stabilized at ~ 1.22 m/s and ~ 365 K, respectively.

2.8 Validation of Computational Models

To verify the accuracy of the numerical simulation model result, the numerical results were compared with the experimental data. The air temperature was used as the criterion for additional comparisons (Román-Roldán et al., 2019). By computing the mean deviation (% error), reduced chi-square value (χ^2), and root mean square error (RMSE) as follows, the correctness of the model suggested to depict the actual system was confirmed:

$$\text{Error (\%)} = \frac{100}{n} * \sum_{i=1}^{i=n} \frac{(T_{E,i} - T_{n,i})^2}{T_{E,i}} \quad (16)$$

$$\chi^2 = \frac{\sum_{i=1}^{i=n} (T_{E,i} - T_{n,i})^2}{n-N} \quad (17)$$

$$RMSE = \sqrt{\frac{\sum_{i=1}^{i=n} (T_{E,i} - T_{n,i})^2}{n}} \quad (18)$$

where n and N stand for the number of observations and degrees of freedom, $T_{E,i}$ is the experimental temperature in Kelvin, and $T_{n,i}$ is the temperature that the numerical model predicted in Kelvin.

3 Results and Discussion

Figure 3 displays the temperature distribution along the inner wall of the drying chamber. The simulation results indicated that the temperature in the solar energy-based PV drying system ranged from 300 to 393 K. The highest temperature (393 K) was observed at the entrance of the drying chamber due to its proximity to the heat source. Furthermore, the simulation results demonstrated that the drying chamber maintains a high temperature through heat convection and conduction from the heating element via the PV system. The heating element produced a constant drying chamber temperature of 365 K. It can be seen that the temperature distribution within the drying chamber was homogeneous. This is a clear indication that the drying system would be capable of consistently and evenly transferring and distributing heat. A consistent drying chamber temperature is essential for drying agricultural products, as it ensures high quality and uniform drying. The maximum drying chamber temperature recorded in this study was 365 K, very close to the 363 K temperature considered suitable for the start of fish drying. At the exit of the drying chamber, a lower temperature was observed, indicating the cooling effect of the surrounding ambient air. This is in agreement with the previous report (Alonge & Obayopo, 2019). The uniform drying chamber temperature of 365 K under no-load conditions is ideal for drying most

agricultural products, as it ensures a superior, consistent drying process. Therefore, it can be inferred that current dryer designs can maintain consistent drying chamber temperatures for most agricultural products, fish, and other seafood.



Fig. 3. Temperature profile of the drying system

The air velocity profile in the drying system is shown in Figure 4. The heated air flows from the heating element into the drying chamber and then exits through the outlet holes on the chamber cover. An investigation of the velocity profile is necessary to understand the airflow pattern, which influences the product's drying rate. The Figure shows that the air velocity in the drying chamber ranged from 0 to 1.55 m/s. These air velocity values were very close to 0.38 m/s reported for the drying chamber of a solar biomass hybrid dryer (Dhanushkodi et al., 2015). The highest air velocity of 1.55 m/s was found at the inlet area because of its closeness to the blower. The obtained simulated velocity values were within the range of 0.6 and 3 m/s, which guarantees a reduction in drying time (Román-Roldán et al., 2019). The results show that the same airflow velocity pattern persisted in some parts of the drying chamber, especially along the inner wall opposite the air inlet. This may be a result of the drying chamber's wall position, air recirculation, and drying air density changes.

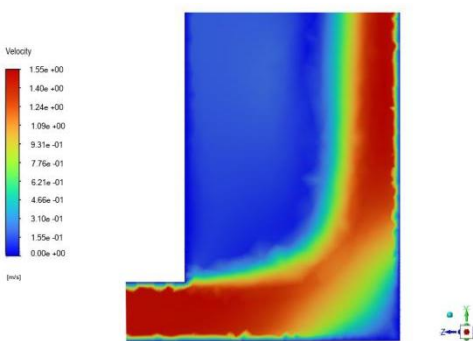


Fig. 4. Velocity profile of the drying system

Figure 5 shows the plot of average temperatures and solar radiation against time at no load condition of the

drying system. As shown in the graphs, solar radiation increased steadily as the day progressed toward 13:00 hr, then declined in the evening. The maximum temperature corresponding to the peak radiation of 754 W/m² for the drying chamber, outlet, and ambient was 386, 349, and 304.9 K respectively. These values were very close to 389, 350.3, and 303.5 K (Komolafe, 2023). During the initial phase of the experiment, the drying chamber temperature increased over time as the space continued to be heated. However, between 14:00 and 16:00, the temperature in the drying chamber remained nearly constant because the PV system supplying heat to the drying chamber maintained a steady level even as insolation decreased. Thus, this scenario is likely to persist until the drying chamber temperature stabilises. The temperature inside the drying chamber ranged from 360 to 386 K. Overall, the drying chamber maintained a higher temperature than the surrounding environment during the experiments. The designed drying system increased the chamber air temperature above ambient levels, making it suitable for drying cocoa beans, cassava slices, apples, peppers, locust beans, vegetables, cereal grains, and various other agricultural products.

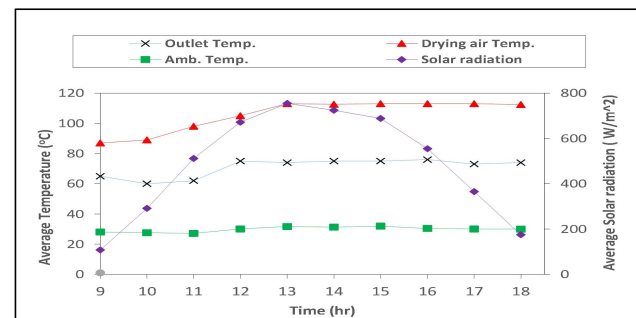


Fig. 5. Plot of average dryer temperatures and solar radiation with time at no load condition of the drying system

Figure 6 depicts the plot of average drying chamber air velocity with time at no load condition of the drying system. The graph shows that the average velocity ranged from 1.36 to 1.40 m/s. The closeness of the values may be attributed to the constant blower speed during the experiments.

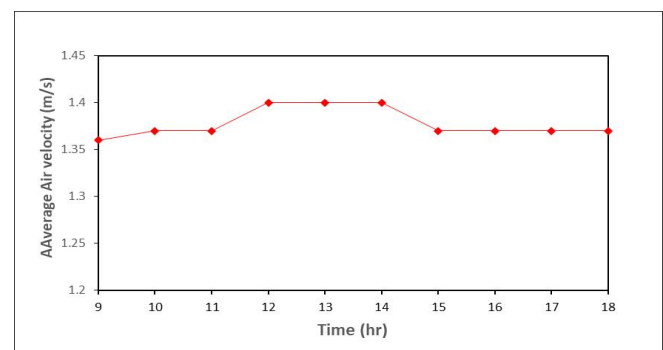


Fig. 6. Plot of average drying chamber air velocity with time at no load condition of the drying system

3.1 Validation of CFD results

The % error (mean deviation) between the experimental and the simulated results was 0.4615%. The obtained RMSE value was 1.0312. With the significance level of 0.05 and the calculated chi-square (χ^2) value of 1.1337. It was observed that the difference between the experimental data and the numerical values is not significant. The obtained mean deviation, chi-square and RMSE values are in tandem with the similar studies by (Komolafe, 2023; Román-Roldán et al., 2019)

Figure 7 further shows the comparison between the experimental and numerical temperature values. The numerical temperature values within the drying system ranged from 92 to 120 °C, while the experimental values ranged from 87 to 113 °C. In general, the Figures show that the numerical and experimental values for the drying systems agree.

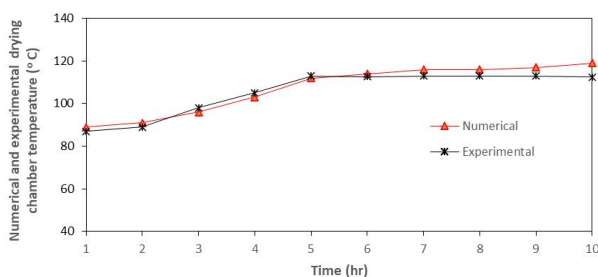


Fig. 7. Comparison of experimental and numerical results for the drying system

4 Conclusion

This study explored the application of Computational Fluid Dynamics (CFD) for both numerical simulation and experimental analysis of 3D simultaneous heat and mass transfer in a forced convection drying system. Fluid flow equations in the drying chamber were solved with the Finite Volume Method using ANSYS Fluent software. Temperature values in the chamber, ranging from 300 to 393 K, were compared with experimental measurements between 360 and 386 K, showing good agreement at peak temperatures. The simulated air velocity of 1.55 m/s closely matched the experimental value of 1.40 m/s. The findings support using these drying systems as viable alternatives to traditional open sun drying, since numerical results are within acceptable ranges. The positive outcomes also indicate that 3D heat and mass transfer models can aid in developing more efficient equipment for processes like drying, cooking, frying, and roasting. Overall, the results confirm that CFD tools are

crucial for designing, analyzing, and optimizing thermal equipment for both household and industrial uses.

References

1. Agbor, M. E., Udo, S. O., Ewona, I. O., Nwokolo, S. C., Ogbulezie, J. C., & Amadi, S. O. (2023). Potential impacts of climate change on global solar radiation and PV output using the CMIP6 model in West Africa. *Cleaner Engineering and Technology*, 13, 100630.
2. Alonge, O. I., & Obayopo, S. O. (2019). Computational fluid dynamics and experimental analysis of direct solar dryer for fish. *Agricultural Engineering International: CIGR Journal*, 21(2).
3. Alqatamin, A., & Jinzhan, S. (2025). Numerical analysis and design of photovoltaic-thermal (PVT) system with novel water-cooling channel structure integrated with perforated V-shape fins. *Renewable energy*, 243, 122587.
4. Chouchane, H., Hassani, S., Mekhilef, S., Lekbir, A., Mubin, M., & Tey, K. S. (2025). A novel ribbed photovoltaic thermal solar dryer with phase change materials: Thermal regulation and drying performance. *Journal of Energy Storage*, 122, 116380.
5. Chukwujindu, N. S. (2017). A comprehensive review of empirical models for estimating global solar radiation in Africa. *Renewable and Sustainable energy reviews*, 78, 955-995.
6. Dhanushkodi, S., Wilson, V. H., & Sudhakar, K. (2015). Simulation of solar biomass hybrid dryer for drying cashew kernel. *Pelagia Research Library Advances in Applied Science Research*, 6(8), 148-154.
7. Dhonde, M., Sahu, K., & Murty, V. (2022). The application of solar-driven technologies for the sustainable development of agriculture farming: a comprehensive review. *Reviews in Environmental Science and Bio/Technology*, 21(1), 139-167.
8. Hammami, M., Torretti, S., Grimaccia, F., & Grandi, G. (2017). Thermal and performance analysis of a photovoltaic module with an integrated energy storage system. *Applied Sciences*, 7(11), 1107.
9. Komolafe, C. A. (2023). Numerical simulation of the 3D simultaneous heat and mass transfer in a forced convection solar drying system integrated with thermal storage material. *Journal of Solar Energy Engineering*, 145(5).
10. Komolafe, C. A., Oluwaleye, I. O., Awogbemi, O., & Osuke, C. O. (2019). Experimental investigation and thermal analysis of solar air heater having rectangular rib roughness on the absorber plate. *Case Studies in Thermal Engineering*, 14, 100442.
11. Komolafe, C. A., Waheed, M. A., Ezekwem, C., & Hii, C. L. (2022). Numerical Analysis of Three-Dimensional Heat and Mass Transfer in Cocoa Beans Under a Solar Drying Condition With a Thermal

- Storage Material. *Journal of Thermal Science and Engineering Applications*, 14(7).
12. Launder, B. E., & Spalding, D. B. (1983). *The numerical computation of turbulent flows*. In *Numerical prediction of flow, heat transfer, turbulence and combustion* (pp. 96-116). Elsevier.
 13. Lemus-Mondaca, R. A., Vega-Gálvez, A., Zambra, C. E., & Moraga, N. O. (2017). Modeling 3D conjugate heat and mass transfer for turbulent air drying of Chilean papaya in a direct contact dryer. *Heat and Mass Transfer*, 53(1), 11-24.
 14. Rabah, A. B., Hemis, M., Ali, L. S., Panigrahi, S. S., Houria, M., Igbozulike, A. O., & Raghavan, V. (2025). Photovoltaic-thermal hybrid solar drying of Chamomilla nobile flowers. *Journal of Stored Products Research*, 114, 102755.
 15. Rani, P., & Tripathy, P. (2023). CFD coupled heat and mass transfer simulation of pineapple drying process using mixed-mode solar dryers integrated with flat plate and finned collector. *Renewable energy*, 217, 119210.
 16. Román-Roldán, N. I., López-Ortiz, A., Ituna-Yudonago, J. F., García-Valladares, O., & Pilatowsky-Figueroa, I. (2019). Computational fluid dynamics analysis of heat transfer in a greenhouse solar dryer “chapel-type” coupled to an air solar heating system. *Energy Science & Engineering*, 7(4), 1123-1139.
 17. Romero, V., Cerezo, E., Garcia, M., & Sanchez, M. (2014). Simulation and validation of vanilla drying process in an indirect solar dryer prototype using CFD Fluent program. *Energy Procedia*, 57, 1651-1658.
 18. Saha, C. K., Roy, N. K., Khatun, J., Tasnim, N., & Alam, M. S. (2024). Solar hybrid dryers for fruits, vegetables, and fish: A comprehensive review on constructional features and techno-economic-environmental analysis. *Sustainable Energy Technologies and Assessments*, 68, 103878.
 19. Tuncer, A. D., Khanlari, A., Afshari, F., Sözen, A., Çiftçi, E., Kusun, B., & Şahinkesen, İ. (2023). Experimental and numerical analysis of a grooved hybrid photovoltaic-thermal solar drying system. *Applied Thermal Engineering*, 218, 119288.
 20. Utomo, B., Darkwa, J., Du, D., & Worall, M. (2025). Solar photovoltaic cooling and power enhancement systems: A review. *Renewable and Sustainable energy reviews*, 216, 115644.
 21. Variava, J. M., Ratnadhariya, J. K., Siddiqui, M. I. H., & Sadasivuni, K. K. (2024). 3D numerical model of a concentrated photovoltaic thermal (CPV/T) system for thermal and electrical performance optimization. *Case Studies in Thermal Engineering*, 61, 104823.
 22. Vásquez, J., Reyes, A., & Pailahueque, N. (2019). Modeling, simulation and experimental validation of a solar dryer for agro-products with thermal energy storage system. *Renewable energy*, 139, 1375-1390.
 23. Vyas, A. A. (2017). CFD Based Thermal Efficiency Analysis of Solar Air Heater with Smooth Plate & Perforated Plate. *Imperial Journal of Interdisciplinary Research*, 3(2).
 24. Wang, X., Wei, L., Hao, W., Wang, L., & Liu, C. (2025). Application evaluation and 4E analysis of PV/T assisted with direct drying chamber system. *Journal of Stored Products Research*, 112, 102645.
 25. Ya’acob, M. E., Hizam, H., Radzi, M. A. M., & Kadir, M. (2013). Field Measurement of PV Array Temperature for Tracking and Concentrating 1 k Wp Generators Installed in Malaysia. *International Journal of Photoenergy*, 2013(1), 502503.
 26. Zambra, C., Moraga, N., Rosales, C., & Lictevout, E. (2012). Unsteady 3D heat and mass transfer diffusion coupled with turbulent forced convection for compost piles with chemical and biological reactions. *International journal of heat and mass transfer*, 55(23-24), 6695-6704.